TITLE: Live-Cell Imaging of NADPH Production from Specific Pathways

AUTHORS: Senlian Hong, Tao Chen, Ling Liu, Chen Cao, Fengxiang Lv, Joshua D. Rabinowitz, Yanyi Huang, and Xing Chen

DOI: 10.31635/ccschem.020.202000346

Live-Cell Imaging of NADPH Production from Specific Pathways

Senlian Hong[1,2,3§,‡], Tao Chen[4,5,6,†,‡], Ling Liu[10,11], Chen Cao[4,5,6], Fengxiang Lv[7], Joshua D. Rabinowitz[10,11], Yanyi Huang*[1,2,3,4,5,6,12], and Xing Chen*[1,2,3,8,9]

[1]College of Chemistry and Molecular Engineering, [2]Peking-Tsinghua Center for Life Sciences, [3]Beijing National Laboratory for Molecular Sciences, [4]College of Engineering, [5]Biomedical Pioneering Innovation Center, [6]Beijing Advanced Innovation Center for Genomics, and [7]Institute of Molecular Medicine, [8]Synthetic and Functional Biomolecule Center, and [9]Key Laboratory of Bioorganic Chemistry and Molecular Engineering of Ministry of Education, Peking University, Beijing, 100871. [10]Lewis-Sigler Institute for Integrative Genomics and [11]Department of Chemistry, Princeton University, Princeton, NJ 08544. [12]Institute for Cell Analysis, Shenzhen Bey Laboratory, Guangdong, 518132, Peking University, Beijing, 100871. [§]S. Hong, Department of Molecular Medicine, The Scripps Research Institute, La Jolla, CA, 92037. [†]T. Chen, Huffington Center on Aging, Baylor College of Medicine, Houston, TX 77030. [‡] These authors contributed equally to this work.

*Corresponding authors: Prof. Yanyi Huang (yanyi@pku.edu.cn) or Prof. Xing Chen (xingchen@pku.edu.cn)

Abstract: As an essential cofactor for lipid biosynthesis and antioxidant defense, NADPH is produced via various pathways, including the oxidative pentose

phosphate pathway (oxPPP) and malic enzyme 1 (ME1). Live-cell detection of NADPH production routes remains challenging. Here we report tracing hydrides into lipid droplets (THILD), a chemical imaging strategy for pathway-specific NADPH in live cells. This strategy exploits deuterium-labeled glucose ([^{2}H]Glc) tracers that transfer deuterides to NADPH via specific pathways. NADP^{2}H in turn transfers deuterides to lipids, resulting in accumulation of C-^{2}H bonds in lipid droplets which can be visualized by bioorthogonal stimulated Raman scattering microscopy. We demonstrate the imaging of oxPPP-produced NADPH using the oxPPP-specific tracer [3-^{2}H]Glc. Furthermore, the switch-on of NADPH production by ME1 in differentiating adipocytes is imaged by [4-^{2}H]Glc. Finally, comparison of [3-^{2}H]Glc and [4-^{2}H]Glc THILD is used to visualize the hypoxia-induced switch off the main NADPH source to oxPPP in adipocytes

Keywords: NADPH, metabolic reprogramming, bio-orthogonal Raman imaging, deuterium tracing, SRS microscopy, pathway-specificity

As a carrier for high-energy electrons, reduced nicotinamide adenine dinucleotide phosphate (NADPH) is an essential cofactor for supplying the reducing power for lipid biosynthesis and maintaining redox homeostasis in living cells. NADPH is produced in various pathways, including the oxidative pentose phosphate pathway (oxPPP), folate metabolism, and malic enzyme 1 (ME1).[1,2] The contribution of different NADPH-producing pathways or enzymes for maintaining cellular physiology is cell type-dependent and varies in response to the redox status of cells. Aberrant NADPH metabolism has been implicated in various health conditions, such as cancer and aging.[3-5] Therefore, detection and quantification of cellular NADPH pools are of great importance for understanding a variety of important biochemical and pathological processes.

Currently, fluorescence microscopy and mass spectrometry (MS) are two complementary approaches for NADPH analysis, each of which has its own strengths and limitations. NADPH can be directly visualized in live cells by using fluorescence lifetime imaging microscopy (FLIM), which exploits the characteristic fluorescence lifetime of the nicotinamide ring in its enzyme-bound state.[6] Moreover, genetically encoded and semisynthetic fluorescent sensors have recently been developed for imaging and quantifying NADPH concentrations in living cells.[7,8] Fluorescent imaging allows for analysis of the overall NADPH at the live single-cell level, however, it cannot differentiate NADPH made by different production pathways. Alternatively, NADPH can be

isotopically labeled in a pathway-specific manner by using stable isotope tracers and MS detection with MS.[9] Specifically, deuterium (^{2}H)-labeled glucose ([^{2}H]Glc) tracers have been used to report the transfer of the deuterium-labeled hydride (i.e., deuteride) to NADPH, resulting in deuterium-labeled NADPH (i.e., NADP^{2}H). For example, [3-^{2}H]Glc can serve as a tracer for detecting NADPH produced by the oxPPP. The deuteride at carbon-3 (C-3) is transferred to NADP^{2}H by the oxPPP enzyme 6-phosphogluconate dehydrogenase (6PGD), and NADP^{2}H can be detected and quantified by liquid chromatography (LC)-MS.[10,11] Similarly, [4-^{2}H]Glc specifically reports on NADP^{2}H produced by the malic enzyme.[12] Although providing pathway specificity, the MS-based measurements have to be performed in cell extracts made from many cells.

Herein we report the development of tracking hydrides into lipid droplets (THILD), a chemical imaging strategy for pathway-specific visualization of NADPH in live cells (Figure 1). THILD employs stimulated Raman scattering microscopy (SRS)[13] to visualize carbon-deuterium (C-^{2}H) bonds in lipid droplets (LDs), for which the deuteride is transferred from NADP^{2}H during fatty acid synthesis. By using pathway-specific [^{2}H]Glc tracers, Raman imaging of LDs therefore reports on the production of NADPH from respective pathways. Unlike the conventional NADPH analysis methods based on fluorescence microscopy and MS, THILD combines the strengths of both to offer an integrative solution.

Specific chemical bonds such as C-^{2}H possess a Raman scattering within the Raman-silent region of a cell between ~1,900 cm^{-1} and ~2700 cm^{-1}. Because endogenous biomolecules do not produce any Raman signal in this silent region, these chemical bonds can be exploited as bioorthogonal Raman reporters to tag biomolecules for live-cell imaging.[14,15] Although NADP^{2}H could in principle be directly imaged by Raman microscopy, it remains practically challenging because of the intrinsically weak signal. Even with SRS which greatly improves the detection sensitivity of spontaneous Raman spectroscopy,[13] the cellular concentration of NADPH (~100 μM)[16] is below the detection limit. To solve this problem, THILD exploits fat synthesis, the most NADPH-demanding pathway that transfers and accumulates deuteride of NADP^{2}H to the C-^{2}H bonds of lipids in LDs. Because of the extremely high lipid concentration in LDs,[17] the C-^{2}H signal is highly enriched in LDs and exceeds that of other deuterium-labeled molecules in cells, thus enabling specific SRS imaging of LDs with high contrast.

We first sought to demonstrate THILD by imaging oxPPP-produced NADPH using [3-^{2}H]Glc as the tracer. Lipogenesis is NADPH-dependent and therefore accumulates C-^{2}H on newly synthesized fatty acids and cholesterol,[10,11] which are major components of LDs.[17] HepG2 cells, a human hepatic cell line with active lipogenesis, were incubated with [3-^{2}H]Glc for 2 d. The spontaneous Raman spectra of [3-^{2}H]Glc-treated cells exhibited a C-^{2}H peak at ~2145 cm^{-1}, which fell into the silent region and therefore was not interfered by intrinsic

Raman signals of cellular molecules (Figure 2a, Figure S1). SRS spectra showed the C-^{2}H peak at the same frequency, confirming the specificity of SRS microscopy at 2145 cm^{-1} for C-^{2}H in live cells (Figure 2a, Figure S2). The [3-^{2}H]Glc-treated cells were stained with BODIPY to visualize LDs,[18] which were then imaged by SRS microscopy and confocal fluorescence microscopy (Figure 2b). Spherical droplets delimited by the SRS signal of C-^{2}H colocalized well with the C-H SRS signal at 2845 cm^{-1}, which has been widely used to visualize lipid droplets.[19-21] Taken together, these results demonstrate that catabolism of [3-^{2}H]Glc results in accumulation of C-^{2}H in LDs, which can be directly visualized by SRS microscopy at 2145 cm^{-1}.

We further validated that THILD imaging using [3-^{2}H]Glc can specifically manifest the NADPH production via the oxPPP pathway. There are several pathways through which [^{2}H]Glc can transfer deuterides to metabolites used for lipogenesis: (i) through glycolysis, the ^{2}H can be transferred to glycerol 3-phosphate (G3P), (ii) the glycolysis-produced pyruvate can enter the mitochondria and transfers ^{2}H to acetyl-CoA (AcCoA), which can be transported to the cytoplasm via the citrate shuttle, (iii) through the oxPPP pathway, ^{2}H can be transferred to NADPH. With NADPH and AcCoA used in the fatty acid synthesis and G3P in the triglyceride synthesis during lipogenesis, the three metabolites link Glc catabolism with packaging triglycerides within LDs (Figure S3a). For [3-^{2}H]Glc, the ^{2}H at C-3 is transferred to NADPH and G3P, but not AcCoA (Figure 2c, Figure S3b). To quantify the contribution of the THILD signal

in LDs from individual metabolites, we employed the LC-MS method[10,11] to track deuterium transfer in the [3-^{2}H]Glc-treated cell lysates (Figure 2c). About 25% NADPH was labeled with deuterium and about 18% G3P labeled (Figure 2d). As expected, AcCoA was not labeled. We also confirmed that ^{2}H was effectively transferred into fatty acids, including myristate, palmitate, and stearate (Figure 2e). The results were in agreement with the previous data[10,11], with slight variations on labeling ratios attributable to differences in cell lines and incubation time. Biosynthesis of one molecule of glycerol tripalmitate (as an example), it consumes 52 molecules of NADPH and 1 molecule of G3P, resulting in their contributions of ^{2}H in glycerol tripalmitate to be 98.7% and 1.3%, respectively (Figure S3c). With the C-^{2}H SRS signals in LDs mostly from NADPH, [3-^{2}H]Glc THILD can be used to probe NADPH production by the oxPPP pathway in live cells.

To normalize the variation of lipid concentration within different LDs, we defined THILD intensity as the proportion of C-^{2}H bonds in the total carbon-hydrogen bonds including C-^{2}H and C-H bonds, which can be calculated by [C-^{2}H]/([C-^{2}H]+[C-H]) (see Experimental Procedures). We then obtained THILD distribution in each cell (Figure 2b, bottom-right panel). The NADPH production via oxPPP in HepG2 cells could be readily visualized by THILD using [3-^{2}H]Glc at 1 d and the THILD signal accumulated to saturation at 2 d (Figure 2f). When the [3-^{2}H]Glc-treated cells were chased in normal media containing Glc, the THILD signal was mostly lost within 1 d (Figure 2g). In addition, THILD

signal could be diminished by inhibition of fatty acid synthase (Figure 2h). These results demonstrate the turnover of lipogenesis from Glc is at the time scale of several days, which is well suited for THILD.

Next, we expanded the tracer repertoire to various [^{2}H]Glc molecules for THILD imaging in HepG2 cells (Figure 3a). Based on the biochemical reactions in the conversion of glucose to lipids, different [^{2}H]Glc tracers have distinct capabilities on transferring deuterides to NADPH, AcCoA, and G3P (Figure S3b). LC-MS analysis confirmed the ^{2}H transfer profiles of [^{2}H]Glc and revealed the labeling ratios of three metabolites (Figure 3b) and fatty acids (Figure S4). [1-^{2}H]Glc produced THILD signals from all three metabolites. [2-^{2}H]Glc and [4-^{2}H]Glc only labeled G3P, resulting in a weak THILD signal. [5-^{2}H]Glc did not resulted in G3P labeling as shown by LC-MS, probably due to signal loss by deuterium exchange with H_2O in the step of conversion of glyceraldehyde 3-phosphate (GAP) to dihydroxyacetone phosphate (DHAP). [6,6-$^2H_2$]Glc labeled G3P and AcCoA and detectable THILD signals were observed. [U-$^2H_7$]Glc with all C-H bonds substituted with deuterium exhibited strong THILD signals and is well suited for SRS imaging of de novo lipogenesis.[22] Similar results were observed in LNCap and Raw264.6 cells, demonstrating the generic applicability of THILD in various cell types (Figure S5).

To further demonstrate the versatility of THILD, we exploited the combination of two tracers, [4-^{2}H]Glc and [3-^{2}H]Glc, to visualize NADPH production in adipocytes (Figure 4a-b). In adipocytes, ME1 and ATP citrate

lyase are upregulated, which together with malate dehydrogenase can synthesize NADPH from NADH.[23] ME1 is a major NADPH producer in adipocytes but not pre-adipocytes, as determined by LC-MS using metabolic tracers including [4-^{2}H]Glc.[12] We then applied THILD to detect this switch of NADPH production pathways by live-cell imaging. 3T3-L1 preadipocytes were differentiated into adipocytes, and the two types of cells were used for comparison. Since [4-^{2}H]Glc-labeled G3P contributes insignificantly to lipid labeling comparing to NADPH, [4-^{2}H]Glc can serve as a THILD tracer specific for ME1-produced NADPH. As expected, in 3T3-L1 preadipocytes [3-^{2}H]Glc THILD signals corresponding to oxPPP-produced NADPH were detected, but no malic enzyme-produced NADPH was observed in [4-^{2}H]Glc THILD imaging (Figure S6a).

Upon differentiation to adipocytes, strong [4-^{2}H]Glc THILD signals were observed, indicating switch-on of the ME1-mediated NADPH production (Figure 4a). By comparing the [4-^{2}H]Glc THILD signal to the [3-^{2}H]Glc THILD signal, the relative contributions of ME1 and oxPPP to NADPH production are at an about 1:1 ratio, with oxPPP being a little less (Figure 4b). In hypoxia, ME1 in adipocytes is downregulated, thus switching NADPH production toward oxPPP.[12] Accordingly, comparison of THILD [4-^{2}H]Glc and [3-^{2}H]Glc imaging revealed that NADPH production from ME1 was greatly suppressed and oxPPP-produced NADPH became the dominant source in adipocytes in hypoxia (Figure 4c,d).

In summary, we have developed a chemical imaging strategy, THILD, for monitoring cellular NADPH production routes. THILD combines two features: live-cell detection and pathway specificity. Other current methods provide only one of these features. For example, MS-based methods cannot be performed in live cells and fluorescence microscopy-based approaches do not differentiate NADPH from different pathways. THILD provides a new way to investigate NADPH-related cellular metabolism pathways in live cells, which is complementary to the current methods. For example, fluorescence microscopy-based methods offer direct visualization of NADPH, which enables monitoring of the dynamics changes of NADPH with better time resolution.

In principle, THILD can be applied to detect other metabolites. For example, [6,6-$^2H_2$]Glc labels AcCoA and G3P (Figure S3b). Because synthesizing a molecule of glycerol tripalmitate uses 24 AcCoA molecules and 1 G3P molecule (Figure S3c), [6,6-$^2H_2$]Glc can likely serve as an AcCoA-specific tracer. In addition, [4-^{2}H]Glc labels cytosolic NADH, which is upstream of NADPH (Figure 4a). It is an interesting future direction to investigate these metabolism pathways in live cells using THILD. Of note, SRS currently has a detection limitation on C-^{2}H in the mM range, which limits the detection sensitivity of THILD. With future improvements on the sensitivity of SRS, THILD may be applied to monitor faster dynamics in cellular metabolism.

Supporting Information

The Supporting Information is available (Additional figures, materials and methods)

Conflict of interest

The authors declare no conflict of interests

Acknowledgments

This project is supported by the National Natural Science Foundation of China (No. 91753206 and No. 21521003 for X.C; No. 21327808 and No. 21525521 for Y.H.), the National Key R&D Program of China (No. 2018YFA0507600 to X.C. and 2018YFA0108100 to Y.H.), 2018 Beijing Brain Initiation (Z181100001518004 to Y.H.), Beijing Advanced Innovation Center for Genomics (to Y.H.), US National Institutes of Health (R01CA163591 to J.D.R.), and China Postdoctoral Science Foundation (2015M580009 to S.H.).

References

1. Ying, W. NAD+/NADH and NADP+/NADPH in cellular functions and cell death: regulation and biological consequences. *Antioxid. Redox Signal.* **2008**, 10, 179–206.
2. Lunt, S. Y.; Vander Heiden, M. G. Aerobic glycolysis: meeting the metabolic requirements of cell proliferation. Annu. *Rev. Cell Dev. Biol.* **2011**, 17, 441–464.

3. Jeon, S. M.; Chandel, N. S.; Hay, N. AMPK regulates NADPH homeostasis to promote tumour cell survival during energy stress. *Nature* **2012**, 485, 661–665.

4. Patra, K. C.; Hay, N. The pentose phosphate pathway and cancer. *Trends Biochem. Sci*. **2014**, 39, 347–354.

5. Nóbrega-Pereira, S.; Fernandez-Marcos, P. J.; Brioche, T.; Gomez-Cabrera, M. C.; Salvador-Pascual, A.; Flores, J. M.; Vina, J.; Serrano, M. G6PD protects from oxidative damage and improves healthspan in mice. *Nat. Commun*. **2016**, 7, 10894.

6. Blacker, T. S.; Mann, Z. F.; Gale, J. E.; Ziegler, M.; Bain, A. J.; Szabadkai, G.; Duchen, M. R. Separating NADH and NADPH fluorescence in live cells and tissues using FLIM. *Nat. Commun*. **2014**, 5, 3936.

7. Tao, R.; Zhao, Y.; Chu, H.; Wang, A.; Zhu, J.; Chen, X.; Zou, Y.; Shi, M.; Liu, R.; Su, N.; Du, J.; Zhou, H. M.; Zhu, L.; Qian, X.; Liu, H.; Loscalzo, J.; Yang, Y. Genetically encoded fluorescent sensors reveal dynamic regulation of NADPH metabolism. *Nat. Methods* **2017**, 14, 720–728.

8. Sallin, O.; Reymond, L.; Gondrand, C.; Raith, F.; Koch, B.; Johnsson, K. Semisynthetic biosensors for mapping cellular concentrations of nicotinamide adenine dinucleotides. *Elife* **2018**, 7, 783.

9. Jang, C.; Chen, L.; Rabinowitz, J. D. Metabolomics and Isotope Tracing. *Cell* **2018**, 273, 822–837.

10. Fan, J.; Ye, J.; Kamphorst, J. J.; Shlomi, T.; Thompson, C. B.; Rabinowitz, J. D. Quantitative flux analysis reveals folate-dependent NADPH production. *Nature* **2014**, 510, 298–302.

11. Lewis, C. A.; Parker, S. J.; Fiske, B. P.; McCloskey, D.; Gui, D. Y.; Gree, C. R.; Vokes, N. I.; Feist, A. M.; Vander Heiden, M. G.; Metallo, C. M. Tracing compartmentalized NADPH metabolism in the cytosol and mitochondria of mammalian cells. *Mol. Cell* **2014**, 55, 253–263.

12. Liu, L.; Shah, S.; Fan, J.; Park, J. O.; Wellen, K. E.; Rabinowitz, J. D. Malic enzyme tracers reveal hypoxia-induced switch in adipocyte NADPH pathway usage. *Nat. Chem. Biol.* **2016**, 12, 345–352.

13. Cheng, J. X.; Xie, X. S. Vibrational spectroscopic imaging of living systems: An emerging platform for biology and medicine. *Science* **2015**, 350. aaa8870–aaa8870.

14. Hong, S.; Lin, L.; Xiao, M.; Chen, X. Live-cell bioorthogonal Raman imaging. *Curr. Opin. Chem. Biol.* **2015**, 24, 91–96.

15. Shen, Y.; Hu, F.; Min, W. Raman Imaging of Small Biomolecules. *Annu. Rev. Biophys.* **2019**, 48, 347–369.

16. Lu, W.; Wang, L.; Chen, L.; Hui, S.; Rabinowitz, J. D. Extraction and quantitation of nicotinamide adenine dinucleotide redox cofactors. *Antioxid. Redox Signal.* **2018**, 28, 167–179.

17. Olzmann, J. A.; Carvalho, P. Dynamics and functions of lipid droplets. *Nat. Rev. Mol. Cell Biol.* **2019**, 20, 137–155.

18. Listenberger, L. L.; Brown, D. A. Fluorescent detection of lipid droplets and associated proteins. *Curr. Protoc. Cell Biol.* John Wiley & Sons, Inc: New York, United States, 2007.

19. Freudiger, C. W. Min, W.; Saar, B. G.; Lu, S.; Holtom, G. R.; He, C.; Tsai, J. C.; Kang, J. X.; Xie, X. S. Label-free biomedical imaging with high sensitivity by stimulated Raman scattering microscopy. *Science* **2008**, 322, 1857–1861.

20. Wang, M. C.; Min, W.; Freudiger, C. W.; Ruvkun, G.; Xie, X. S. RNAi screening for fat regulatory genes with SRS microscopy. *Nat. Methods* **2011**, 8, 135–138.

21. Dou, W.; Zhang, D.; Jung, Y.; Cheng, J. X.; Umulis, D. M. Label-free imaging of lipid-droplet intracellular motion in early Drosophila embryos using femtosecond-stimulated Raman loss microscopy. *Biophys. J.* **2012**, 102, 1666–1675.

22. Li, J.; Cheng, J. X. Direct visualization of de novo lipogenesis in single living cells. *Sci. Rep.* **2014**, 4, 6807.

23. Wise, L. S.; Sul, H. S.; Rubin, C. S. Coordinate regulation of the biosynthesis of ATP-citrate lyase and malic enzyme during adipocyte differentiation. Studies on 3T3-L1 cells. *J. Biol. Chem.* **1984**, 259, 4827–4832 (1984).

Table of Contents Graphic

By combination of bioorthogonal Ramam imaging and isotopic tracing, THILD imaging enables the pathway-specific visualization of NADPH in live cells.

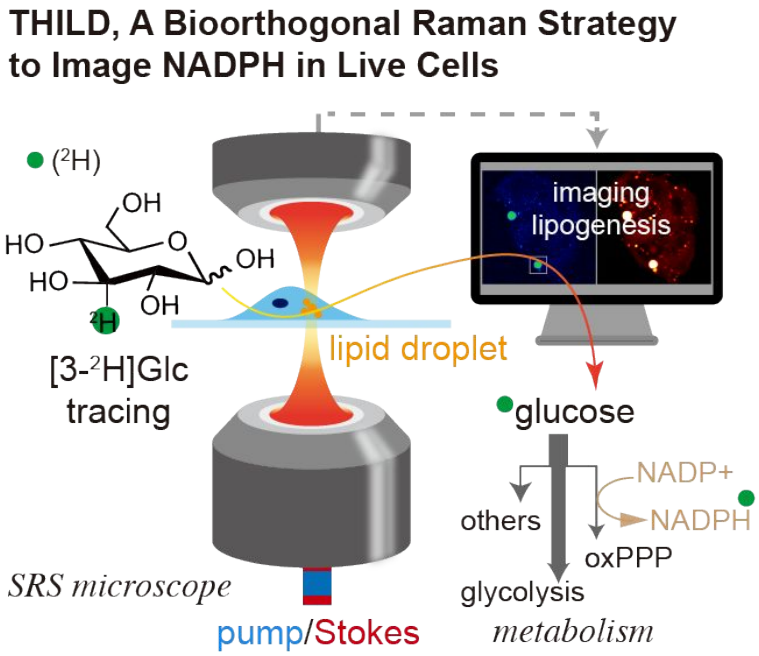

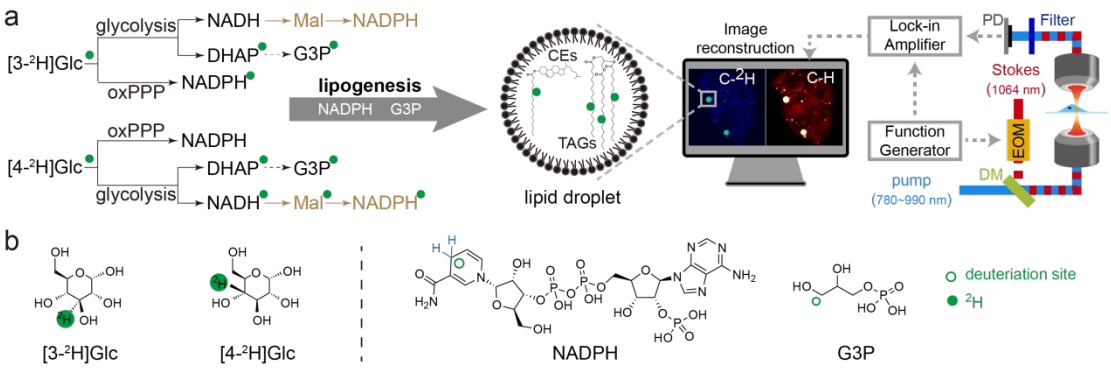

Figure 1. THILD enables pathway-specific imaging of NADPH production in live cells. a) Flow of the deuteride of [3-^{2}H]Glc and [4-^{2}H]Glc to metabolites through glycolysis, oxPPP, and/or ME1. The deuterium-labeled NADPH and G3P are used for lipogenesis, which result in accumulation of C-^{2}H in LDs. Bioorthogonal SRS microscopy at 2145 cm^{-1} for C-^{2}H in LDs, which is termed THILD, hence exhibits NADPH production in living cells. The dash lines indicate insignificant contribution to THILD signal. Note that ME1-mediated production of NADPH is only active in adipocytes but not HepG2 cells. b) Chemical structures of [3-^{2}H]Glc, [4-^{2}H]Glc, NADPH, and G3P.

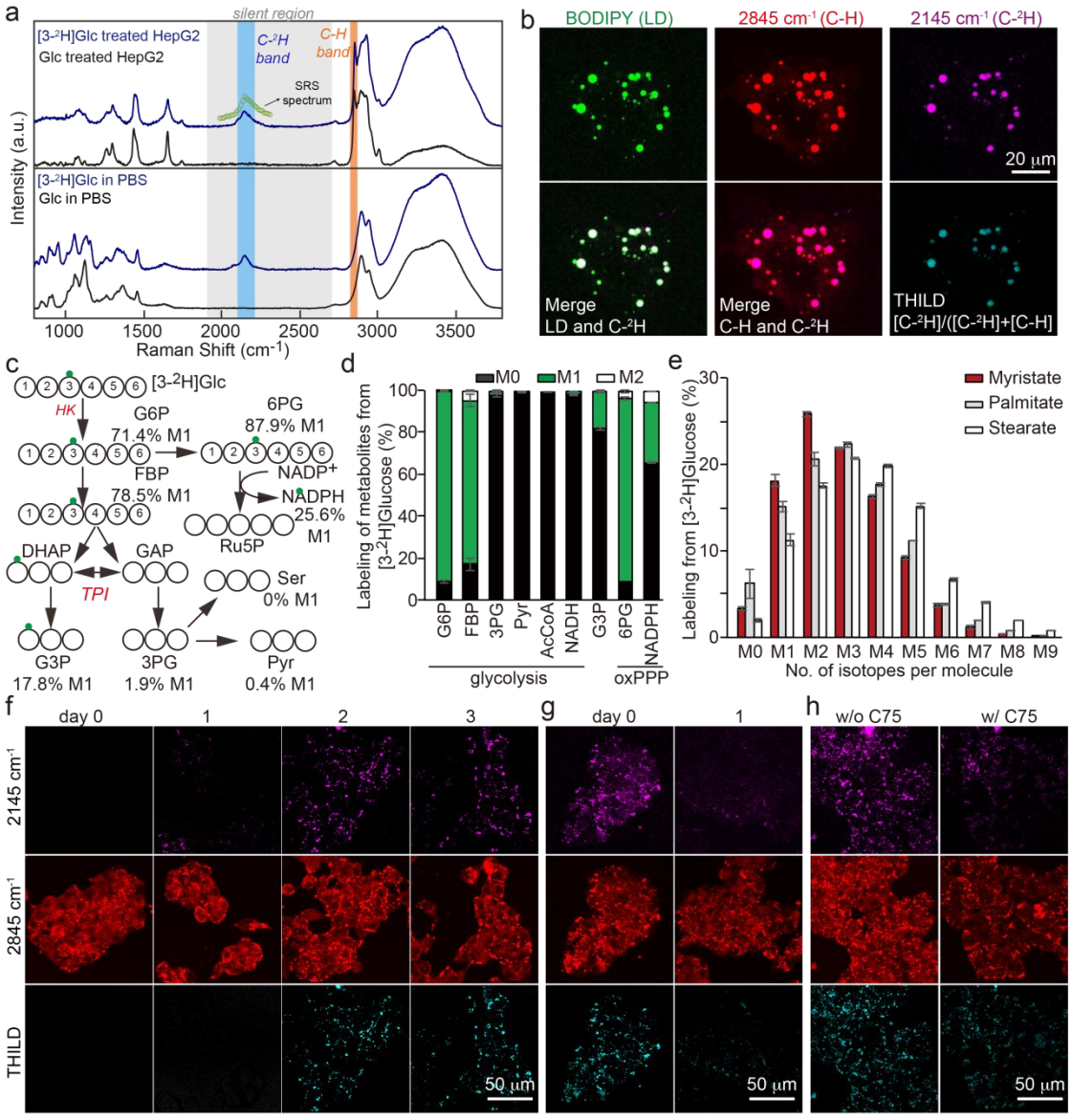

Figure 2. THILD imaging of oxPPP-produced NADPH by [3-²H]Glc in live cells. a) Spontaneous Raman spectra of HepG2 cells cultured in [3-²H]Glc or Glc, and PBS solutions of [3-²H]Glc and Glc. The green curve shows the SRS spectrum mapped from the [3-²H]Glc-treated cells. b) SRS, fluorescence, and THILD images of HepG2 cells treated with 25 mM [3-²H]Glc for 2 d, followed by staining with BODIPY. Scale bar, 20 μm. c) Schematic showing the flow of the [3-²H]Glc hydride through oxPPP and glycolysis. Open circles represent carbon and green dots represent deuterium. The numbers below the metabolites indicate deuterium labeling ratios. d) Labeling of

metabolites in HepG2 cells treated with [3-^{2}H]Glc, followed by analysis by LC-MS. NADPH was measured at 20 min and the rest at 2 h. e) Labeling of fatty acids in HePG2 cells treated with [3-^{2}H]Glc for 2 d. f-h) THILD and SRS images of HepG2 cells treated with 25 mM [3-^{2}H]Glc for varied durations of time (f), incubated with 25 mM [3-^{2}H]Glc for 2 d, followed by chasing with Glc for 1 d, and incubated with 25 mM [3-^{2}H]Glc for 2 d, in the presence and absence of an fatty acid synthase inhibitor C75 (h). For SRS imaging, the channels of C-^{2}H at 2145 cm^{-1} and C-H at 2845 cm^{-1} are shown. In d) and e), error bars represent mean ± s.d. Results are from three independent experiments. In b), f), g), and h), scale bars, 50 μm.

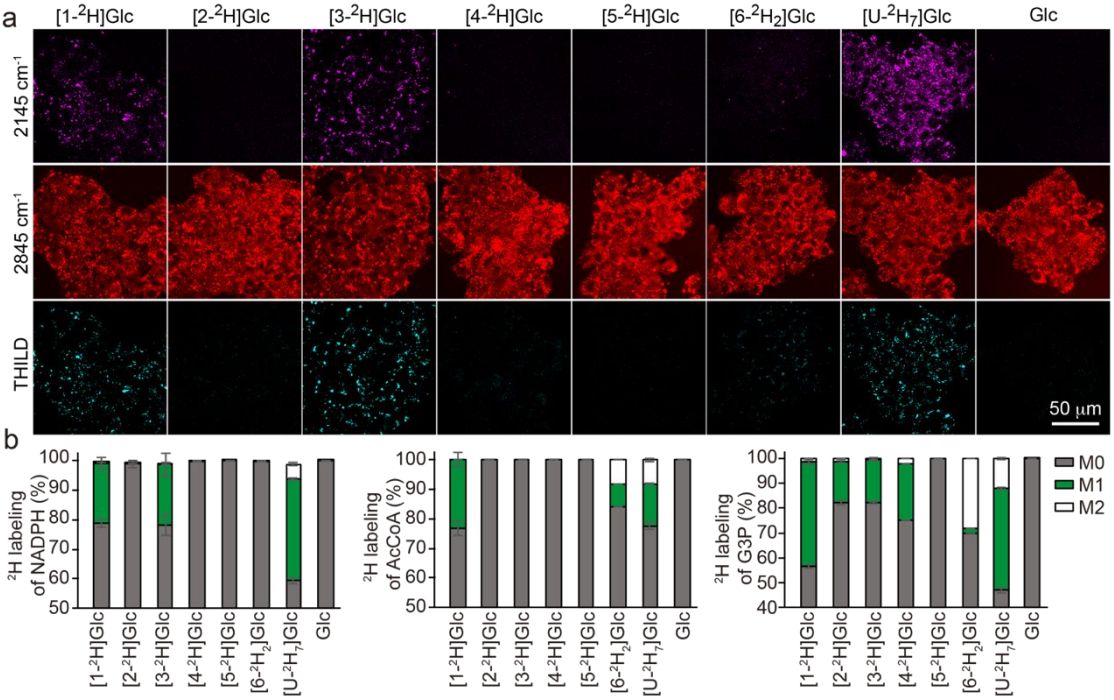

Figure 3. THILD imaging using various [^{2}H]Glc tracers. a) THILD and SRS images of HepG2 cells incubated with 25 mM [1-^{2}H]Glc, [2-^{2}H]Glc, [3-^{2}H]Glc, [4-^{2}H]Glc, [5-^{2}H]Glc, [6,6-$^2H_2$]Glc, [U-^{7}H]Glc, or Glc for 2 d. For SRS imaging, the channels of C-^{2}H at 2145 cm^{-1} and C-H at 2845 cm^{-1} are shown. Scale bar, 50 μm. b) ^{2}H Labeling of NADPH, AcCoA, and G3P from various [^{2}H]Glc tracers at 25 mM in HepG2 cells. NADPH was measured from cells treated with tracers for 20 min and AcCoA and G3P were measured at 2 h by LC-MS. M0, M1, M2 are isotopomers with no, one, and two ^{2}H atoms, respectively. Error bars represent mean ± SD. Results are from three independent experiments.

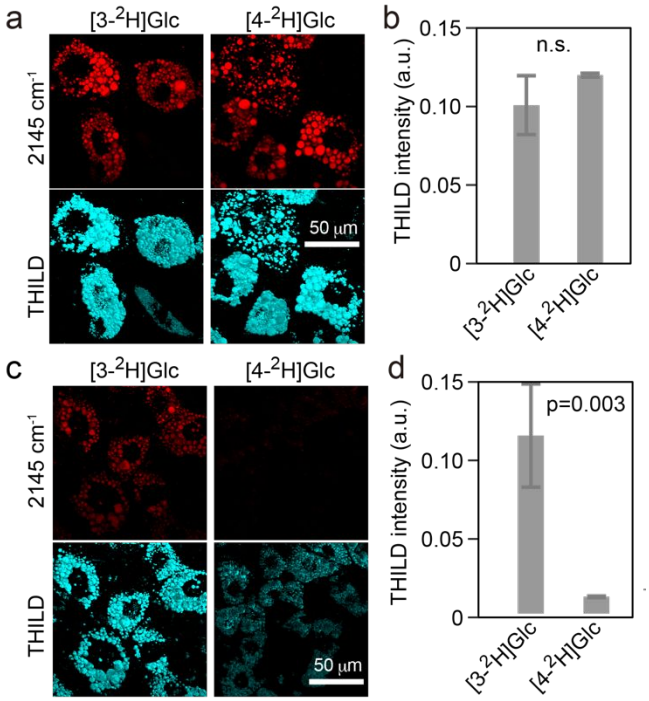

Figure 4. THILD imaging of NADPH production in adipocytes. a,c) THILD and SRS images of differentiating 3T3-L1 adipocytes treated with 25 mM [3-^{2}H]Glc or [4-^{2}H]Glc in conditions of normoxia (a) and hypoxia (c). For SRS imaging, the channel of C-^{2}H at 2145 cm^{-1} is shown. Scale bar, 50 μm. b,d) Statistical analysis of THILD intensity of cells in conditions of normoxia (b) and hypoxia (d). Error bars represent mean ± SD. Results are from at least 10 cells from three independent experiments. The significance was assessed via unpaired two-tailed Student's t-test, and p value was provided. Note, n.s. represents not significant ($p \geq 0.05$) .